

Research paper

## Avoiding cracks in additively manufactured non-weldable directionally solidified Ni-based superalloys

Xiaofeng Dang<sup>a,1</sup>, Yao Li<sup>b,c,1</sup>, Kai Chen<sup>d,\*</sup>, Upadrasta Ramamurty<sup>e</sup>, Sihai Luo<sup>a</sup>,  
Xiaoqing Liang<sup>a</sup>, Weifeng He<sup>a,f,\*\*</sup>

<sup>a</sup> Science and Technology on Plasma Dynamics Laboratory, Air Force Engineering University, Xi'an, Shaanxi 710038, China

<sup>b</sup> School of Materials Science and Engineering, Chang'an University, Xi'an, Shaanxi 710064, China

<sup>c</sup> Key Laboratory of Road Construction Technology & Equipment of Ministry of Education, Chang'an University, Xi'an, Shaanxi 710064, China

<sup>d</sup> Center for Advancing Materials Performance from the Nanoscale (CAMP-Nano), State Key Laboratory for Mechanical Behavior of Materials, Xi'an Jiaotong University, Xi'an, Shaanxi 710049, China

<sup>e</sup> School of Mechanical and Aerospace Engineering, Nanyang Technological University, 639798, Singapore

<sup>f</sup> State Key Laboratory for Manufacturing Systems Engineering, Xi'an Jiaotong University, Xi'an, Shaanxi 710049, China

### ARTICLE INFO

#### Keywords:

Directionally solidified Ni-based superalloys

Electron beam powder bed fusion

Laser directed energy deposition

Cracking prevention

Columnar dendrite growth

### ABSTRACT

Additive manufacturing of directionally solidified Ni-based superalloys faces at least two critical obstacles, namely, the formation of stray equiaxed grains and the susceptibility to cracking; circumventing both of these simultaneously is considered difficult. In this study, a comparative study of a non-weldable superalloy IN738 fabricated through the laser directed energy deposition (DED) without preheating the base plate and the electron beam powder bed fusion (EB-PBF) with preheating up to the upper bound of ductility dip temperature range was performed. With appropriate process parameters, a steep and unidirectional temperature gradient, a sufficiently high cooling rate at the liquid/solid interface, and a relatively low cooling rate at the  $\gamma'$  solvus are obtained simultaneously in the EB-PBF process. The prevalence of these conditions results in the growth of well-aligned columnar dendrites, mitigates the elemental segregation, reduces the built-in microscopic defects, and lowers the stored deformation energy. Consequently, cracking is successfully prevented and reasonable room temperature tensile properties are achieved in the as-printed EB-PBF product. Moreover, recrystallization is not triggered during the post-printing heat treatment, and thus the  $\langle 001 \rangle$  fiber texture is preserved. This study provides a detailed understanding of the critical factors that need to overcome for producing directionally solidified superalloys through additive manufacturing.

### 1. Introduction

Directionally solidified (DS) superalloys are widely used as aircraft engine blades because they possess superior performance at elevated temperatures compared to their polycrystalline analogues, mainly due to the [001] oriented columnar grains and the elimination of transverse grain boundaries. Metal additive manufacturing (AM), also known as 3D printing, promises unprecedented capacity to produce structural components with complex geometries [1–3]. The application of AM to manufacture the DS Ni-based superalloy components is attractive—both from the manufacturing of new components and the repair of those

damaged during service perspectives—and hence garnered considerable interest over the past couple of decades. However, only a few successful cases have been reported so far [4–6]. This is because of the following two major challenges, (i) prevention of cracking [7–9] and (ii) precise control over the orientation of the columnar grains [10]. As schematically illustrated in Fig. 1, nearly opposite temperature gradients all essential for meeting these two conditions can be satisfied, as detailed below.

\* Corresponding author.

\*\* Corresponding author at: Science and Technology on Plasma Dynamics Laboratory, Air Force Engineering University, Xi'an, Shaanxi 710038, China.

E-mail addresses: [kchenbl@gmail.com](mailto:kchenbl@gmail.com) (K. Chen), [hehe\\_coco@163.com](mailto:hehe_coco@163.com) (W. He).

<sup>1</sup> These authors contributed equally to this work.

<https://doi.org/10.1016/j.addma.2022.103095>

Received 4 May 2022; Received in revised form 2 August 2022; Accepted 16 August 2022

Available online 19 August 2022

2214-8604/© 2022 Elsevier B.V. All rights reserved.

### 1.1. Cracking prevention

Ni-based superalloys with  $\text{Ti} + \text{Al} > 6 \text{ wt}\%$  are considered non-weldable because of their cracking susceptibility during welding [9, 11,12]. Since AM processes such as laser powder bed fusion (L-PBF) and e-beam powder bed fusion (EB-PBF) are akin to welding—in terms of the beam/alloy interactions and the principal mechanisms of solidification that prevails, it is widely acknowledged that the alloys amenable to welding are also those amenable to AM using these techniques. Different cracking mechanisms, generally classified into either hot cracking or solid-state cracking, have been identified in previously published studies on superalloys [8,9,13–15]. The driving force for both these kinds of cracking has origins in the tensile stresses that are caused by the high cooling rates intrinsically associated with the specific AM processes [16], the volume change accompanied by the phase transition from the  $\gamma$ -matrix to the  $\gamma'$ - $\text{Ni}_3(\text{Al}, \text{Ti}, \text{Ta})$  precipitates [17], and the stress field surrounding the built-in structural defects such as vacancies and dislocations. As suggested by prior experimental and numerical investigations [18–20], preheating the base plate to a high homologous temperature is effective to prevent cracking as a consequence of decrease in temperature gradient and thus stresses. Detailed studies indicate that the preheating temperature needs to be similar to or even higher than the ductility-dip temperature range (DTR), which is approximately 50–80 % of the melting temperature ( $T_m$ ) [19,21]. To suppress hot cracking, it is also important to mitigate the elemental segregation between the dendrite cores (DCs) and the interdendritic regions (IRs), so as to prevent the formation of low melting point liquid films.

### 1.2. Columnar dendrite growth

The preservation of the [001] oriented columnar dendritic microstructure aligned with the building direction (BD) is a prerequisite for the AM of DS superalloys. It is thus essential to maintain a sufficiently large ratio of temperature gradient to crystal growth velocity at the liquid/solid interface [22], and a steep temperature gradient parallel to BD, *i.e.*, a shallow melt pool with a large width to depth ratio [23,24]. In this case, the directional growth is realized on a DS or single crystal superalloy base plate whose surface normal is parallel to the crystallographic [001] direction [21,25,26]. Even with a polycrystalline base metal, DS or single crystalline microstructure can be obtained beyond a certain build height [10,27,28], similar to the orientation selection process of the Bridgman method. In some cases, however, a perturbation in the melt pool alters the local solidification conditions [29] and generates stray grains [30], which may induce hot cracking along

high-angle grain boundaries [31,32].

In summary, preheating of the base plate helps suppress the cracks. However, it may also provoke the formation of stray grains by perturbing the steep unidirectional temperature gradient [21]. Recently, multiple possibilities for the successful fabrication of crack-free DS and even single crystalline Ni-based superalloys through EB-PBF with a preheating temperature of  $\sim 1000 \text{ }^\circ\text{C}$  were demonstrated [5,10,27,28]. These results suggest that with the electron-beam heat source, a steep and unidirectional temperature gradient can be achieved despite the high-temperature preheating. However, detailed understanding of the underlying mechanism and a thorough comparison with laser directed energy deposition (DED) are yet to be articulated [33].

In this study, the non-weldable IN738 Ni-based superalloy powders with  $\text{Al} + \text{Ti} > 6.7 \text{ wt}\%$  were used as the feedstock of AM, given that the creep life of IN738 DS turbine blades is superior to their polycrystalline counterparts [34]. Both the EB-PBF and DED approaches were utilized to uncover the essential factors in the fabrication of crack-free DS grain architecture. A comparative study of melt pool geometry, dendrite morphology, grain orientation, elemental segregation, solidification constituents, and dislocation density in the as-printed samples produced through the two AM methods was conducted. Their resistances to recrystallization during the post-printing solutionizing heat treatment were evaluated. On the basis of these results, the mechanism and practical solutions for overcoming the two major challenges facing the AM of DS superalloys were proposed.

## 2. Materials and experimental methods

Gas atomized IN738 superalloy powders with the nominal composition of Ni-0.10 C-0.01B-16.1Cr-3.51Al-3.23Ti-8.49Co-2.09Ta-2.67 W-1.83Mo-0.84 Nb (wt%) and a diameter range of 45–105  $\mu\text{m}$  were used as the feedstock for both the EB-PBF and the DED processes. Polished polycrystalline 304 stainless steel plates were employed as the substrates. As shown in Fig. S1 in the Supplementary Material, a wide range of processing parameters were first explored to minimize the density of internal defects such as cracks, pores, and the lack of fusion defects. Once the crack-free products were obtained using the EB-PBF process, the printing parameters were further refined to achieve directional dendrite growth. The optimized process parameters for both the approaches employed in this study are listed in Table 1.

The DED experiments were carried out with a coaxial powder feeding apparatus equipped with a Nd:YAG laser source. Powders were injected by high-purity argon gas carrier into the melt pool and finally a bulk sample with a size of  $55 \times 25 \times 15 \text{ mm}^3$  was fabricated with the layer thickness of 500  $\mu\text{m}$ , as shown in Fig. 2b. No preheating was utilized

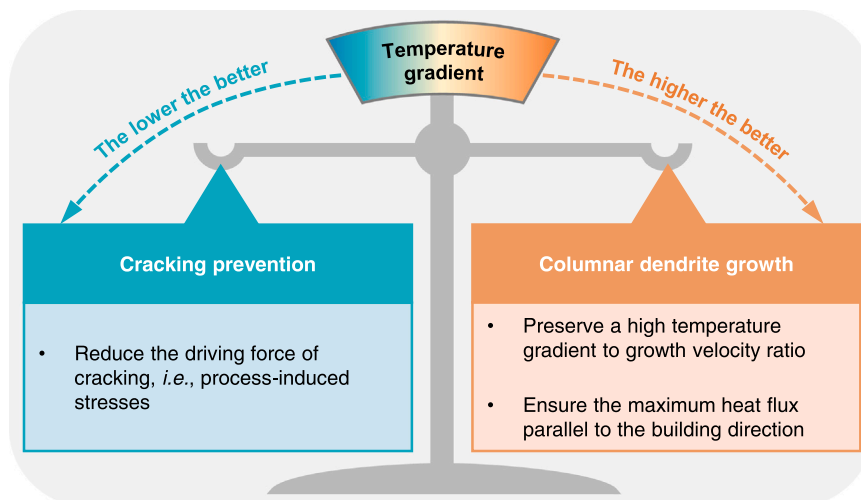


Fig. 1. Major challenges faced by the AM of non-weldable DS Ni-based superalloys.

**Table 1**  
Optimized processing parameters used for the EB-PBF and DED samples.

Method	Preheating temperature (°C)	Scanning speed (mm·s <sup>-1</sup> )	Beam diameter (mm)	Input power (W)
DED	25	7	2.5	1200
EB-PBF	950 ± 30	4000	0.6	600

during the DED process.

EB-PBF experiment was carried out in a selective electron beam melting machine (Sailong-S200) at a constant accelerating voltage of 60 kV under a vacuum pressure of  $4 \times 10^{-2}$  Pa. A bulk EB-PBF sample of  $50 \times 10 \times 20$  mm<sup>3</sup> (Fig. 2e) was produced with the layer thickness of 50 μm. Taking account of the DTR of IN738 to be 509–978 °C evaluated from its solidus temperature of 1291 °C [35], a preheating temperature of (950 ± 30) °C was maintained during the deposition process.

For both DED and EB-PBF, the scanning directions of all the tracks were identical in a certain deposition layer but reversed between adjacent layers, as illustrated in Fig. 2a. To describe the sample geometry, we denoted longitudinal (*i.e.*, parallel or anti-parallel to the heat source scanning direction), transverse, and building directions as X, Y, and Z in this article, respectively. After AM, the YZ planes of samples were mechanically ground and finely polished with a 3.5 μm diamond paste. After electro-etching in aqueous phosphoric acid (30 vol%) at 5 V for 5 s, the samples were investigated by optical microscopy and scanning electron microscopy (SEM, Hitachi SU6600) under both secondary electron (SE) and backscattered electron (BSE) imaging modes. The element distribution was examined by using the electron probe micro-analysis (EPMA, JEOL SuperProbe JXA-8230) and the energy dispersive spectroscopy (EDS) at an accelerating voltage of 20 kV. Electron backscattered diffraction (EBSD, Bruker e-Flash XS) equipped in a SEM (Zeiss EVO10) was used to map the grain orientations in the two samples with an identical scan area ( $1150 \times 860$  μm<sup>2</sup>) and step size (4 μm). The EBSD samples were prepared by electrochemical polishing in a 10 vol% perchloric acid alcohol at the voltage of 25 V for about 20 s. For the detailed analysis of the microstructure, a combination of transmission electron microscope (TEM, JOEL JEM-2100Plus) and EDS was performed. All the SEM, EBSD, and TEM samples were extracted from the DED and EB-PBF bulk samples at the same build height (~4 mm above the base plate).

To evaluate the mechanical properties, dog-bone-shaped tensile specimens with a gauge length of 20 mm were machined from the as-printed bulk EB-PBF sample (Fig. 2e). The room temperature (RT) uniaxial tensile tests were performed at a constant displacement rate of ~1 mm/min until fracture by using an MTS electronic universal material testing machine (INSTRON M4206). Because the dense cracks in the DED sample (Fig. 2b) lead to the failure to machine a tensile specimen, the hardness of the as-printed DED and EB-PBF samples was obtained by averaging of at least 5 measurements through a Vickers microhardness tester (HV-1000) with a loading of 200 gf and a dwelling time of 15 s.

### 3. Results

#### 3.1. Dendrite morphology and grain structure

A crack network orienting along both the longitudinal (X) and the transverse (Y) directions is observed in the as-printed DED sample, regardless of the build height (Fig. 2b). The longitudinal cracks tend to propagate along the centerline of melt pools (Fig. 2c). The width and depth of the melt pool cross-section are measured to be 2.2 mm and 0.7 mm, respectively. Note that cracks prevail in all the DED samples regardless of different processing parameters. An enlarged view in Fig. 2d demonstrates the typical dendritic morphology with an average primary dendrite arm spacing (PDAS) of ~7.7 μm. The dendrite growth direction varies at different locations of the melt pool; some dendrites grew perpendicular to the fusion line while some dendrites exhibit a cross-like morphology orienting close to the out-of-plane direction.

In contrast, no cracks could be detected in the EB-PBF sample (Figs. 2e and f). The melt pools, with the cross-sectional geometry of 0.7 mm width and 0.07 mm depth, are much smaller and shallower than those in the DED sample. As seen in Fig. 2f, elongated columnar grains are aligned along BD and pass through multiple deposition layers. An enlarged micrograph displayed in Fig. 2g shows that each columnar grain consists of bundles of well-aligned dendrites. Because of the high cooling rates inherent to AM severely suppress the growth of secondary dendrite arms, these dendrites are also called cells in some literature. In this study, we do not try to distinguish the terms of “cell” and “dendrite”. The average PDAS of dendrites in EB-PBF sample is measured to be 3.1 μm, less than half the PDAS of the DED sample.

Fig. 3 compares the grain morphology and orientation in the two as-printed samples, obtained by using EBSD method. For the DED sample,

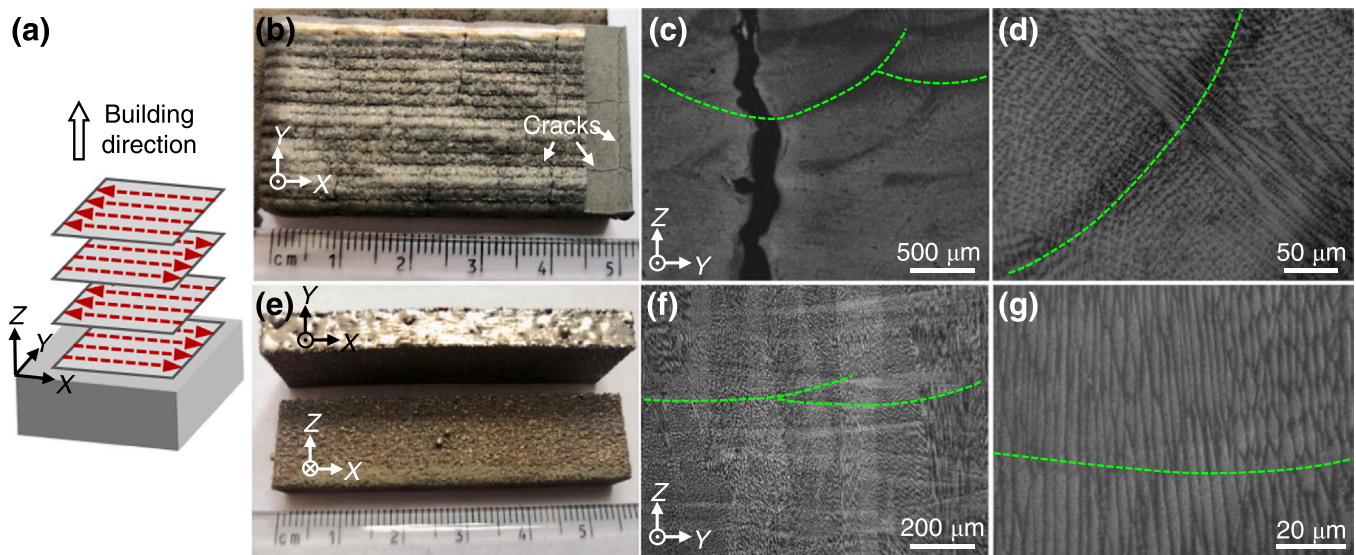


**Fig. 2.** Additive manufacturing of IN738 superalloys through DED and EB-PBF. (a) Schematic illustration of the heat source scanning strategy, in which the scanning directions are illustrated by dashed arrows. As-printed bulk and optical micrographs of vertical cross-sectional samples fabricated by (b-d) DED and (e-g) EB-PBF. Dashed curves in (c-d) and (f-g) indicate the fusion lines.

irregular-shaped grains and an intergranular crack are visible in the inverse pole figure map along BD (IPF-Z map hereafter) in Fig. 3a. The grain orientations are nearly random and show almost no texture (Fig. 3b). The same scenario is also observed in the crack-free region (Fig. S2 in the Supplementary Material). In contrast, the EB-PBF sample consists of columnar grains with preferred elongation direction parallel to BD (Fig. 3c), consistent with the observation in Fig. 2f. The vast majority of grains depicted in red color have an almost identical  $\langle 001 \rangle$  crystallographic direction, resulting in a strong 001 fiber texture along BD (Fig. 3d).

### 3.2. Elemental segregation

The EPMA maps displayed in Fig. 4 present the element distribution at the dendritic scale in the two as-printed samples. The spatial variation in Ti concentration helps identify the dendrite structures, *i.e.*, dendrites growing out of the YZ plane result in cell-like contrast in the DED sample (Fig. 4a), whereas dendrites run parallel to BD in the EB-PBF sample (Fig. 4b). Basically, a similar element partitioning tendency is observed in both the samples, namely,  $\gamma$  forming elements (*e.g.*, Cr and W) partition to DCs,  $\gamma'$  forming elements (*e.g.*, Ti and Al) partition to IRs, and the dispersed nano-sized carbides in the IRs are rich in Ta, Mo, Ti, and W. Unlike the slight segregation of W into DC and Mo into IR in the DED sample, these two elements are more homogeneously distributed in the EB-PBF sample. Figs. 4c and 4d show the concentration fluctuations of Ti and W across multiple dendrites. It is evident that the DED sample exhibits a wider IR and a more severe elemental segregation as compared to the EB-PBF sample. Note that the oxygen concentration in the EB-PBF specimen is notably lower than that in the DED specimen, because the vacuum environment of EB-PBF prevents the deposited

layers from possible high temperature oxidation.

### 3.3. Solidification constituents

As seen in Fig. 5a, the IR of the as-printed DED sample is decorated with carbides and  $\gamma/\gamma'$  eutectics. An enlarged view, shown in Fig. 5b, indicates that the  $\gamma'$  particles in the IR ( $\sim 35$  nm in diameter) are about twice as big as those in the DC ( $\sim 17$  nm in diameter). Particularly, heterogeneous structures consisting of carbide shells and spherical Al-rich oxide cores are frequently observed (Figs. 5a and c), which is consistent with the observed overlaps of the O-rich regions and the carbides in Fig. 4a.

In comparison to the inhomogeneously distributed  $\gamma'$  precipitates in the DED sample, a relatively uniform dispersion of the  $\gamma'$  precipitates in the IR and DC regions is observed in the as-printed EB-PBF sample (Fig. 5d). As indicated in Fig. 5e, the  $\gamma'$  particles in the EB-PBF sample are nearly spherical and much larger than those obtained in the DED sample. The average diameter of the  $\gamma'$  particles in the EB-PBF sample is measured to be  $\sim 152$  nm, although a few smaller  $\gamma'$  particles with sizes down to  $\sim 60$  nm are also found. Besides,  $\gamma/\gamma'$  eutectics and carbide-oxide heterostructures are absent, as suggested by Figs. 5e and f.

### 3.4. Dislocation configurations

TEM investigation was performed to visualize dislocation configurations in the as-printed samples (Fig. 6). The DED sample stores a higher density of dislocations than the EB-PBF sample. By using the line-intercept method [36], the dislocation densities in the DED and the EB-PBF samples were estimated to be  $6.0 \times 10^{13}$  and  $1.8 \times 10^{13} \text{ m}^{-2}$ , respectively. The emergence of superlattice peaks in the selected area

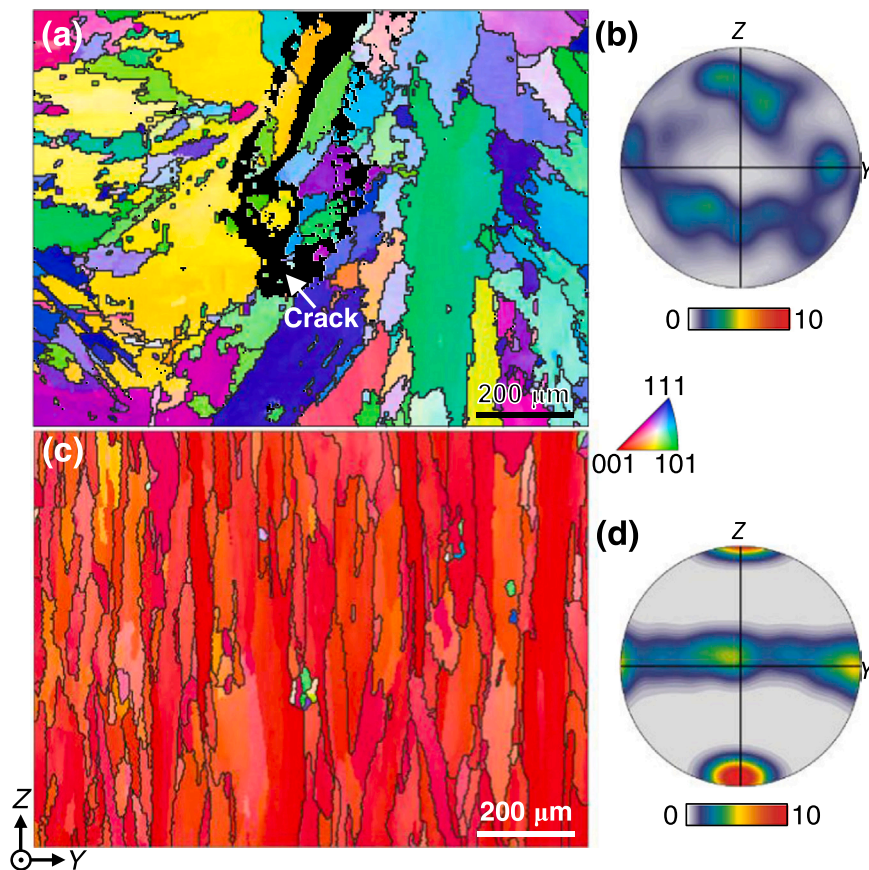


**Fig. 3.** Grain structure of the as-printed DED and EB-PBF samples. EBSD IPF-Z maps and the corresponding 001 pole figures of the as-printed (a-b) DED and (c-d) EB-PBF samples. Two EBSD scans were acquired at the same build height of  $\sim 4$  mm. Black pixels in (a) are those unsolved spots near the crack.

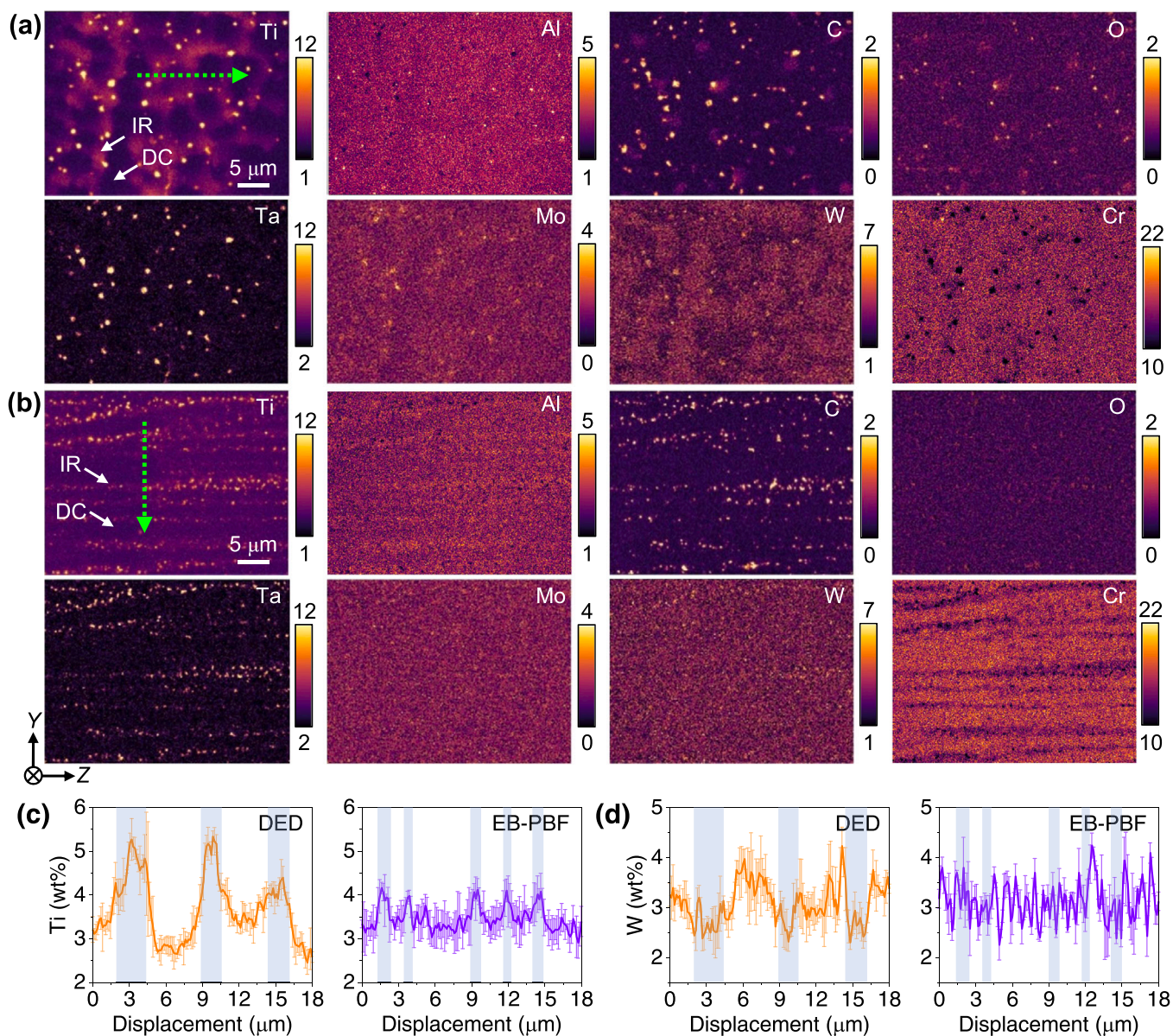


**Fig. 4.** Element distribution in the as-printed DED and EB-PBF samples. EPMA element composition (wt%) maps collected from (a) the DED and (b) the EB-PBF samples. Linear profiles showing the concentration variances of (c) Ti and (d) W. Individual profiles represent averages of five parallel lines near the dotted arrows highlighted on Ti maps in (a) and (b), respectively. The shadows in (c-d) indicate the interdendritic region.

diffraction pattern, shown in the inset of Fig. 6a, confirms the existence of the  $\gamma'$  phase in the as-printed DED sample, although it is nearly indiscernible in the BF-TEM images due to its small size. Due to the size-dependent dislocation-carbide interaction mechanisms, carbides in both samples act as strong barriers to mobile dislocations, evidenced by dislocation looping (Fig. 6b), pinning, and bowing (Fig. 6c) behaviors. Besides, a low angle grain boundary (LAGB) composed of dislocations is also observed in the DED sample (Fig. 6b).

### 3.5. Mechanical properties

The uniaxial tensile tests on the EB-PBF sample (XY plane) at RT were carried out with the loading direction along the X-axis. A yield strength  $\sigma_{YS}$  of 1037.6 MPa, ultimate tensile strength  $\sigma_{UTS}$  of 1210.9 MPa, and uniform elongation  $\epsilon_{UE}$  of 10.3% were obtained (Fig. 7). The inset chart in Fig. 7 presents a comparison of  $\sigma_{UTS}$  and elongation to failure with the previously reported IN738 properties [5, 14,37–39]. Significantly, the mechanical properties of the EB-PBF

sample in this work are superior to its DED and cast counterparts, and comparable to the reported values for EB-PBF IN738 alloys in the literature. Moreover, the average microhardness measured on the EB-PBF sample ( $522.2 \pm 10.8$  HV) is much higher than that measured on the DED sample ( $424.6 \pm 9.2$  HV).

## 4. Discussion

In the previous section, it has been demonstrated that a simultaneous achievement of directional growth of columnar dendrites and crack prevention is realized through the EB-PBF approach. The underlying mechanisms are discussed in the following.

### 4.1. Columnar dendrite growth

#### 4.1.1. Magnitudes of temperature gradient and growth velocity

Although *in-situ* investigations of the morphological evolution of melt pool during AM have been exploited [40,41], experimental

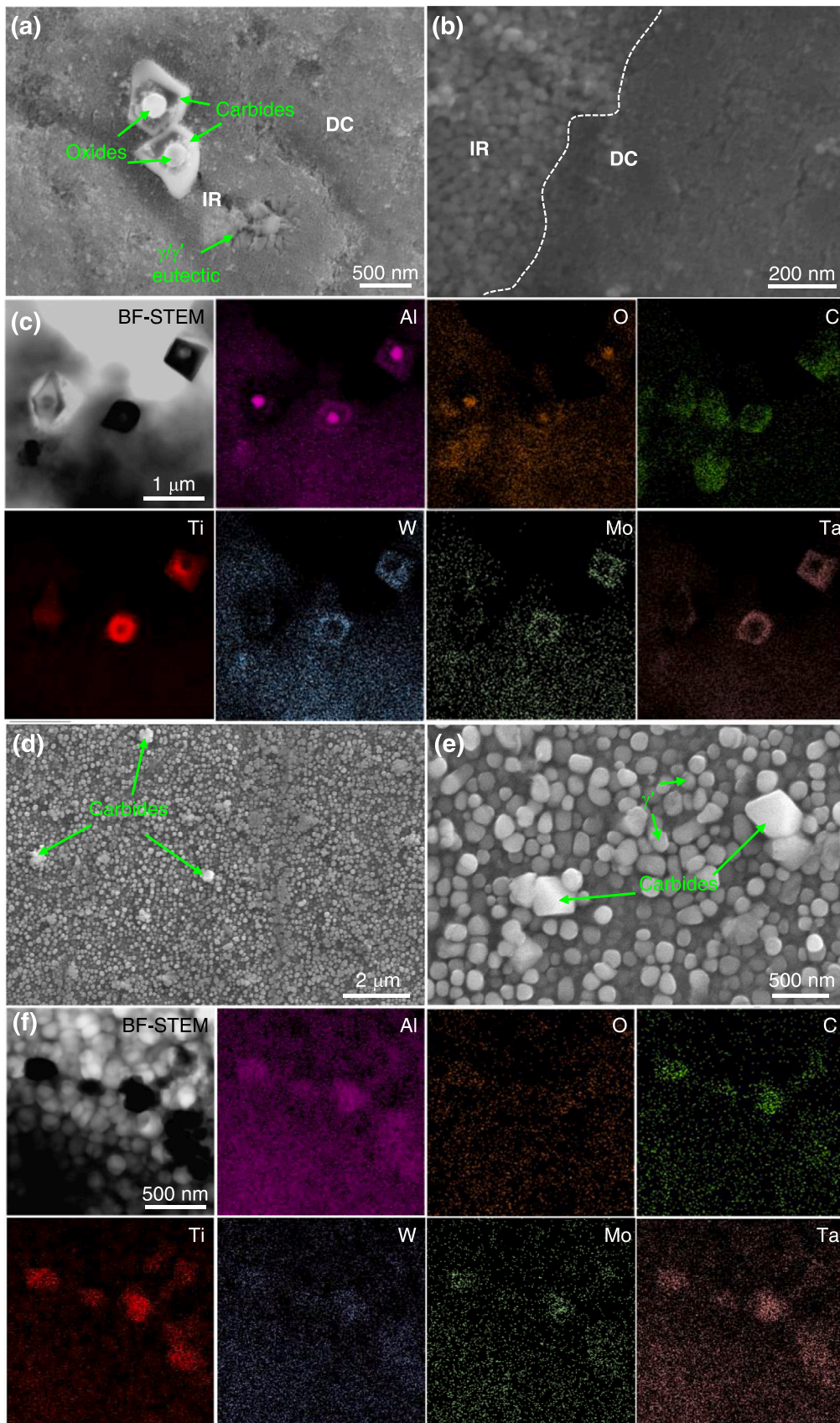


**Fig. 5.** Solidification constituents in the as-printed DED and EB-PBF samples. SE-SEM images showing the distribution of solidification constituents in the (a-b) DED and (d-e) EB-PBF samples. Bright-field (BF) scanning TEM (STEM) images and the corresponding EDS maps showing the element distribution of the carbides in the (c) DED and (f) EB-PBF samples.

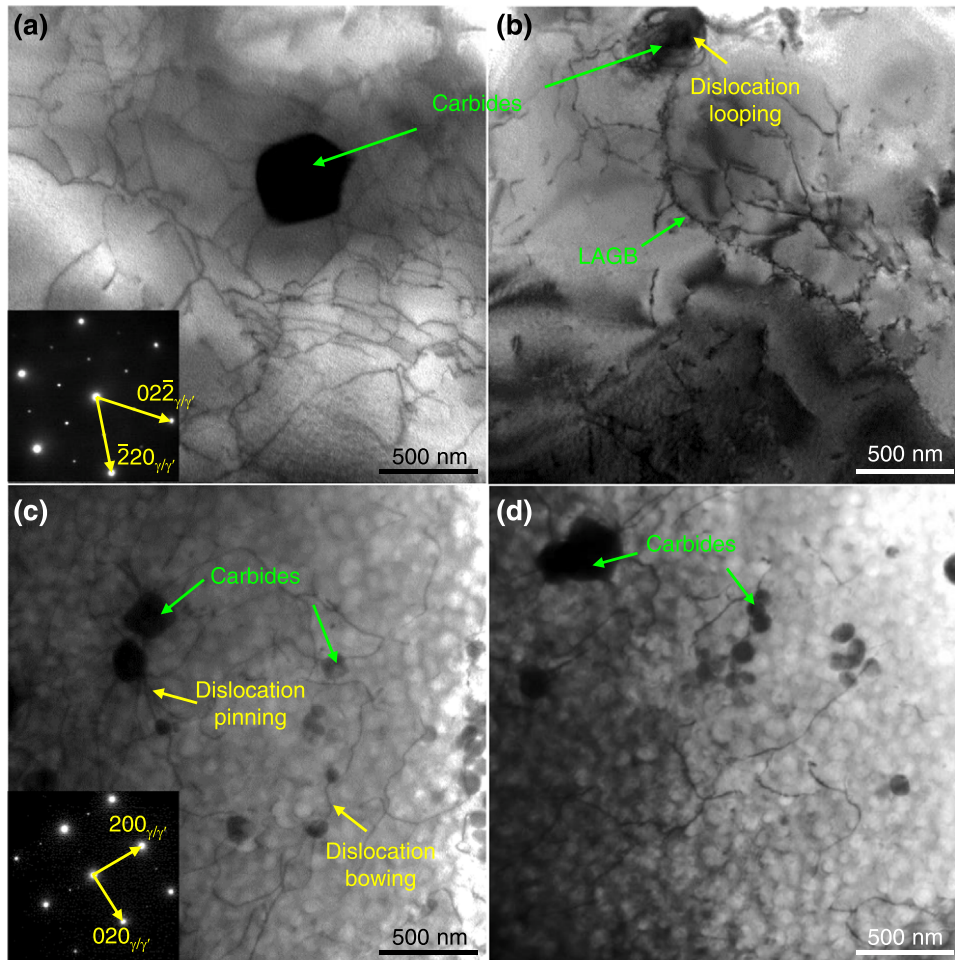


Fig. 6. TEM investigation of the as-printed DED and EB-PBF samples. Dislocation configurations in (a-b) the DED sample along [111] zone axis and (c-d) the EB-PBF sample along [001] zone axis, respectively.

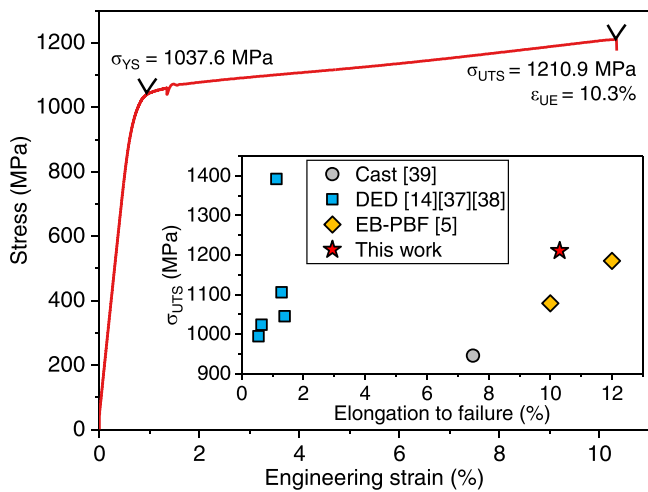


Fig. 7. Stress-strain curve of the room temperature tensile test of the as-printed EB-PBF sample. Inset showing the comparison with other IN738 alloys fabricated by DED [14,37,38], EB-PBF [5], and conventional casting [39] reported in the literature.

measurements of the temperature gradient ( $G$ ) and growth velocity ( $V$ ) remain challenging. The current knowledge of how  $G$  and  $V$  affect the solidification microstructure in the AM alloys is mainly based on simulations and empirical models. To elucidate the stray grain formation

mechanism in additively manufactured superalloys, Gäumann et al. [21] postulated the condition for the dendritic growth under the prevailing rapid solidification conditions as:

$$\frac{G^n}{V} = a \left[ \sqrt[3]{\frac{-4\pi N_0}{3 \ln(1-\phi)} \frac{1}{n+1}} \right]^n \quad (1)$$

where  $N_0$  is the number of nucleation sites,  $a$  and  $n$  are the material-dependent parameters, and  $\phi$  is the local volume fraction of stray grains and site-dependent in the melt pool. An area-weighted average fraction  $\phi$  is used to assess  $\phi$  value over the entire melt pool [42]. Approximate estimates of  $G$  and  $V$  are utilized in the present study by using  $N_0 = 2 \times 10^{15} \text{ m}^{-3}$ ,  $a = 1.25 \times 10^6 \text{ K}^{3.4} \cdot \text{m}^{-1} \cdot \text{s}$  and  $n = 3.4$ , which are assumed identical to those reported for the same alloy system fabricated by both DED [21] and EB-PBF [43].

Stray grains are identified if they have a large misorientation ( $> 15^\circ$ ) relative to the single crystal matrix, while this criterion does not work for DS superalloys in which multiple crystal grains are aligned with their [001] crystallographic direction approximately parallel to BD. Raghavan et al. [43] derived the value of  $\phi$  by quantifying the area fraction of equiaxed grains based on a grain aspect ratio filter in a polycrystalline superalloy fabricated by EB-PBF. However, this approach fails to identify misoriented columnar stray grains that grow at a large deviation angle against the common [001] direction of other columnar grains [44]. Consequently, in this study, the stray grains are identified if they deviate in excess of the threshold angle of  $15^\circ$ . The deflection angle

(Fig. 8), defined as the minimum angle between BD and the six  $\langle 001 \rangle$  axes in each grain, is calculated by a home-made software XtalCAMP [45]. Accordingly,  $\phi$  values of the DED and the EB-PBF samples are computed to be 0.91 and 0.04, respectively. The  $\phi$  value of the EB-PBF sample is even smaller than the best columnar dendritic microstructure ( $\phi = 0.05$ ) obtained by Gäumann et al. [21]. Although some fine stray grains relevant to the fluctuations in the solidification conditions [12] are found in the EB-PBF sample (Fig. 3c and Fig. 8b), their low volume fraction makes them acceptable in a DS superalloy [46].

It is widely accepted that PDAS ( $\lambda$ ) can be well predicted in terms of cooling rate at the liquid/solid interface  $C_{l/s}$ , or the multiplication of  $G$  and  $V$ . The relation can be expressed by the following empirical formula [23]:

$$\lambda = bC_{l/s}^{-m} = b(GV)^{-m} \quad (2)$$

where  $b$  and  $m$  are material specific constants and reported to be 131.08 and 0.31 for IN738 superalloy, respectively [34].

Combining Eqs. (3) and (4) enables the estimation of the values of  $G$  and  $V$  at the liquid/solid interface (listed in Table 2), which are in good agreement with those reported in the same alloy fabricated by DED [47]

and EB-PBF [10,48]. It is apparent from Eq. (1) that  $\phi$  is inversely proportional to  $G^n/V$  ratio and  $n$  is larger than 1, suggesting that  $G$  exerts a more dominant influence than  $V$  on the suppression of stray grains. Despite the negative effect of preheating on  $G$ , the smaller melt pool size in the EB-PBF process leads to a higher  $G$  value compared to the DED process. This, in turn, results in a  $G^n/V$  ratio for the EB-PBF process that is about two orders of magnitude larger than that of DED process and facilitates the formation of columnar dendrites.

#### 4.1.2. Temperature gradient direction

During solidification of alloys, dendrite growth is greatly influenced by the heat flow direction, which is dependent on the local radius of curvature or the width-to-depth ratio of the melt pool [23]. Flat melt pool with large radius of curvature or width-to-depth ratio is favored for the dendrite growth along BD. From Fig. 2c and f, the width-to-depth ratios of the melt pool cross-sections of the DED and the EB-PBF samples are estimated to be 3.1 and 10, respectively. The flatter melt pool bottom of the EB-PBF sample introduces a vertically oriented heat flow, which is anti-parallel to BD. It drives the columnar dendrites to grow directionally along BD in the subsequent layer deposited (Fig. 2f and g). In contrast, the 3D distribution of temperature gradients in the DED process, a result of the larger and deeper melt pool, leads to the spatially varying dendrite growth directions (Fig. 2d).

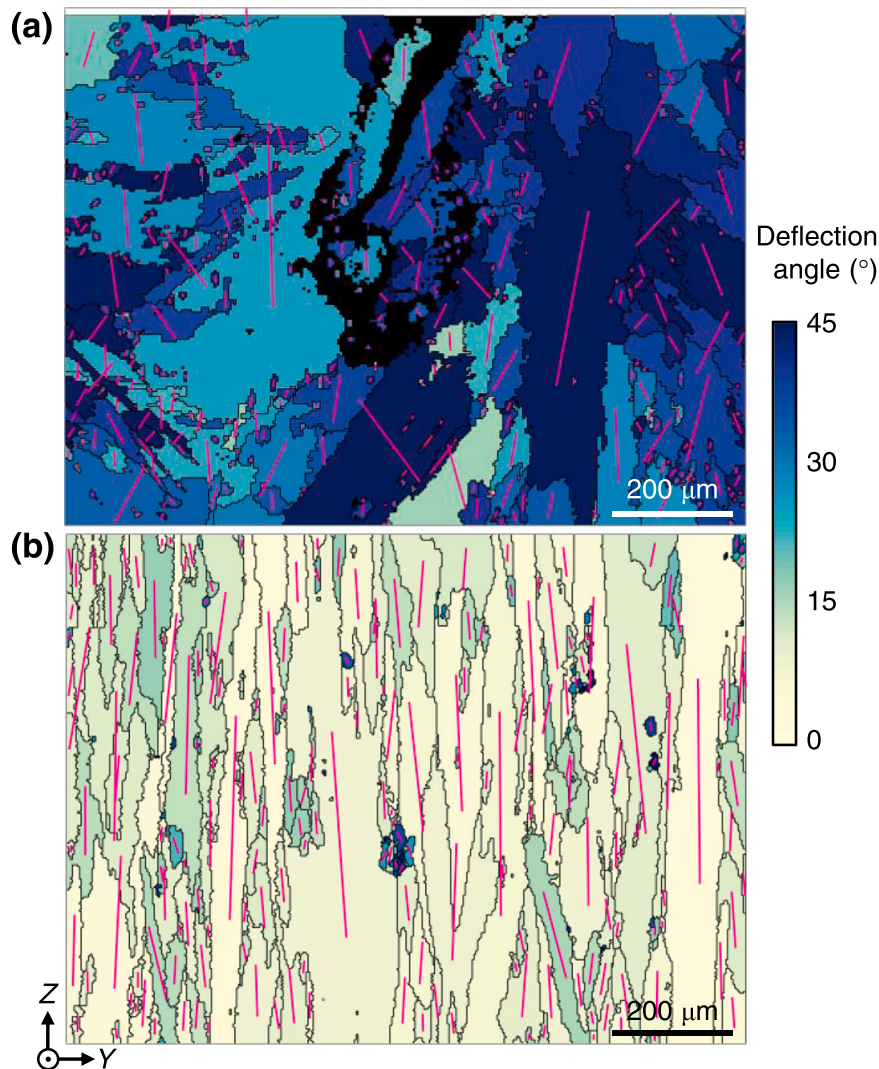


**Fig. 8.** Evaluation of the volume fraction of stray grains. Deflection angle maps of the (a) DED and (b) EB-PBF samples, respectively, obtained from EBSD scans in Fig. 3. The magenta lines delineate the projection of one of the  $\langle 001 \rangle$  axes closest to BD in each grain.

**Table 2**  
Estimation of solidification conditions at the liquid/solid interface.

Method	$\lambda$ ( $\mu\text{m}$ )	$\phi$	$G$ ( $\text{K}\cdot\text{m}^{-1}$ )	$V$ ( $\text{m}\cdot\text{s}^{-1}$ )	$G^{3.4}/V$ ( $\text{K}^{3.4}\cdot\text{m}^{-4.4}\cdot\text{s}$ )	$C_{l/s}$ ( $\text{K}\cdot\text{s}^{-1}$ )
DED	7.7	0.91	$6.2 \times 10^5$	$1.5 \times 10^{-2}$	$3.3 \times 10^{21}$	$9.3 \times 10^3$
EB-PBF	3.1	0.04	$3.5 \times 10^6$	$5.1 \times 10^{-2}$	$3.4 \times 10^{23}$	$1.8 \times 10^5$

The above discussion suggests that an appropriate heat input, which ensures a temperature gradient with a sufficiently large magnitude and a vertically-oriented direction, is critical for the AM of DS superalloys.

## 4.2. Cracking behavior during the DED process

### 4.2.1. Hot cracking

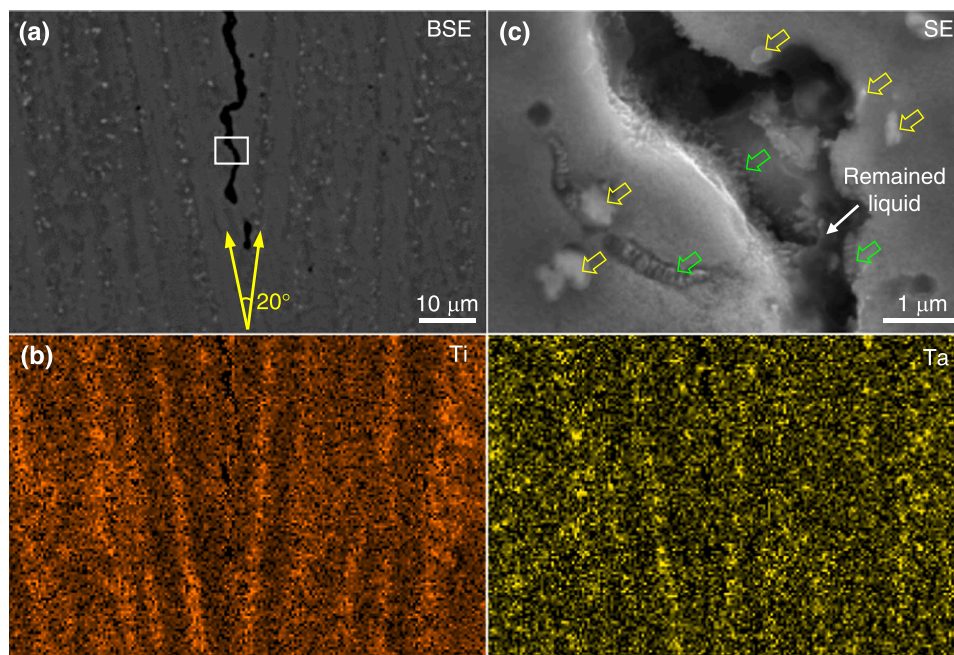
The initiation of hot cracking requires the coexistence of an intergranular low melting liquid film and large tensile stresses. Liquid film originates from either the constitutionally undercooled liquid in the final solidification stage (*i.e.*, solidification cracking) or the remelting of pre-existing low melting phases (*i.e.*, liquation cracking). As seen in Fig. 2d, a longitudinal crack along the centerline of melt pool, similar to the solidification cracking pattern observed in the fusion welding of superalloys [49], occurs. For the layer-wise AM process, however, the discrimination between liquation cracking and solidification cracking is not straightforward, because the solidification path turns out to be very complex under the conditions of melting, remelting, and partial-remelting, *etc.* [9].

Fig. 9a shows that a microcrack initiates and propagates along a grain boundary that is created by the dendrites diverging at an inclination angle of  $\sim 20^\circ$ . Such a grain boundary with misorientation angle larger than a critical value of  $\sim 13^\circ$  has been proven susceptible to hot cracking [50]. As shown in Fig. 9b, the elemental partitioning behavior in this region is the same as Fig. 4. A higher magnification view of the crack indicates the presence of remnant liquid film as well as  $\gamma/\gamma'$  eutectics and carbides along the cracked grain boundary (Fig. 9c).

Given that the grain boundary coincides with IR (Fig. 9a), the element concentrations in the IRs and DCs are further analyzed for both samples. The partitioning coefficient  $k$ , defined as the ratio of

composition in the DC to that in the IR for several alloying elements of IN738, are listed in Table 3. Note that the nominal concentrations of B, C are used because of the inaccurate values provided by EPMA. The degree of partitioning in the EB-PBF sample (with  $k$  values closer to 1) is less significant than that in the DED sample. This is because the cooling rate at the liquid/solid interface ( $C_{l/s}$ ) in the EB-PBF process is about 20 times higher than that in the DED process (Table 2). Based on the chemical compositions listed in Table 3, non-equilibrium thermodynamic calculations based on the Scheil-Gulliver model were performed by using the JMatPro software [51] to simulate the solidification paths (Fig. 10) by retaining only the observed phases, including  $\gamma$ ,  $\gamma'$ , and MC-type carbides. The nominal concentration of carbon is used because of the insufficient accuracy of EPMA for light elements and carbon is omitted when calculating the phase diagrams of DC where carbides are absent. In this way, key temperatures, including the  $\gamma'$  solvus ( $T_{\gamma'}$ ), solidus ( $T_S$ ), and liquidus ( $T_L$ ), are predicted and listed in Table 4. The interdendritic segregation not only lowers the  $T_S$  and  $T_L$  but also enlarges the solidification range ( $\Delta T = T_L - T_S$ ), suggesting the stabilization of the interdendritic liquid film at lower temperatures, which, consequently, enhances the hot cracking susceptibility [52]. Moreover, the interdendritic segregation rises the  $\gamma'$  solvus, and hence  $\gamma'$  particles in the IRs stay in high temperature range for a longer period. Consequently, they grow larger in size than those in DCs of the DED sample (Fig. 5b).

During the layer-wise deposition of DED process, a liquid film may form by complete or partial remelting of grain boundaries and intergranular low melting  $\gamma/\gamma'$  eutectics in the as-deposited layer. The dissolution of MC-type carbides can also contribute to the intergranular liquid film [53]. From the above discussion, the observed intergranular  $\gamma/\gamma'$  eutectics and carbides in Fig. 9c could be a result of the direct solidification from liquid or survived from the partial remelting of the



**Fig. 9.** Hot cracking in the as-printed DED sample. (a) BSE-SEM image showing dendritic microstructure near the initiation and propagation region of a hot crack and (b) the corresponding EDS maps. (c) SE-SEM image showing the enlarged region marked in (a) with carbides and  $\gamma/\gamma'$  eutectics indicated by yellow and green arrows, respectively.

**Table 3**  
Chemical compositions (wt%) of the IR and the DC of DED and EB-PBF samples measured by EPMA.

	Cr	Al	Ti	Co	Ta	W	Mo	Nb	Ni
DED IR	14.62	3.83	5.45	8.07	3.32	2.33	1.73	0.66	59.88
DED DC	16.72	3.6	2.71	8.39	2.41	3.64	1.35	0.56	60.51
$k_{DED}$	1.14	0.94	0.50	1.04	0.73	1.56	0.78	0.85	1.01
EB-PBF IR	14.82	3.88	4.37	8.04	3.21	2.51	1.54	0.64	60.88
EB-PBF DC	16.76	3.43	2.98	8.41	2.54	2.82	1.41	0.61	60.93
$k_{EB-PBF}$	1.13	0.88	0.68	1.05	0.79	1.12	0.92	0.95	1.00

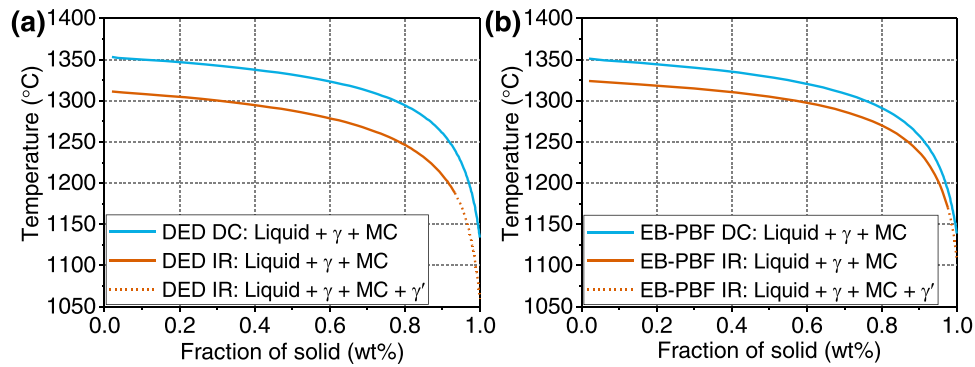


**Fig. 10.** Thermodynamic solidification process calculated using Scheil-Gulliver simulation. The predicted solidification paths of (a) the DED and (b) the EB-PBF samples, based on the compositions of the DC and IR listed in Table 3.

**Table 4**  
Thermodynamic calculations based on the chemical compositions listed in Table 3.

Temperature (°C)	DED IR	DED DC	EB-PBF IR	EB-PBF DC
$\gamma'$ solvus ( $T_\gamma$ )	1188	1124	1175	1129
Solidus ( $T_S$ )	1060	1134	1110	1139
Liquidus ( $T_L$ )	1311	1353	1324	1351
$\Delta T = T_L - T_S$	251	219	214	212

pre-existing solidification products in the as-deposited layer.

Consequently, the solidification cracking and liquation cracking mechanisms are likely to operate simultaneously during the DED process.

4.2.2. Solid-state cracking

In Fig. 11, micrographs of the middle part of another crack in the DED sample are displayed. The crack surface, featuring flat crystallographic facets, is typical of brittle fracture, differing from the hot crack surface with a dendritic morphology [8]. It is thus concluded that this crack initiates through the solid-state cracking mechanism, relevant to either a sudden rise in hardness whilst  $\gamma'$  precipitates (i.e., strain-age cracking) [52] or the intrinsic ductility loss within DTR (i.e., ductility

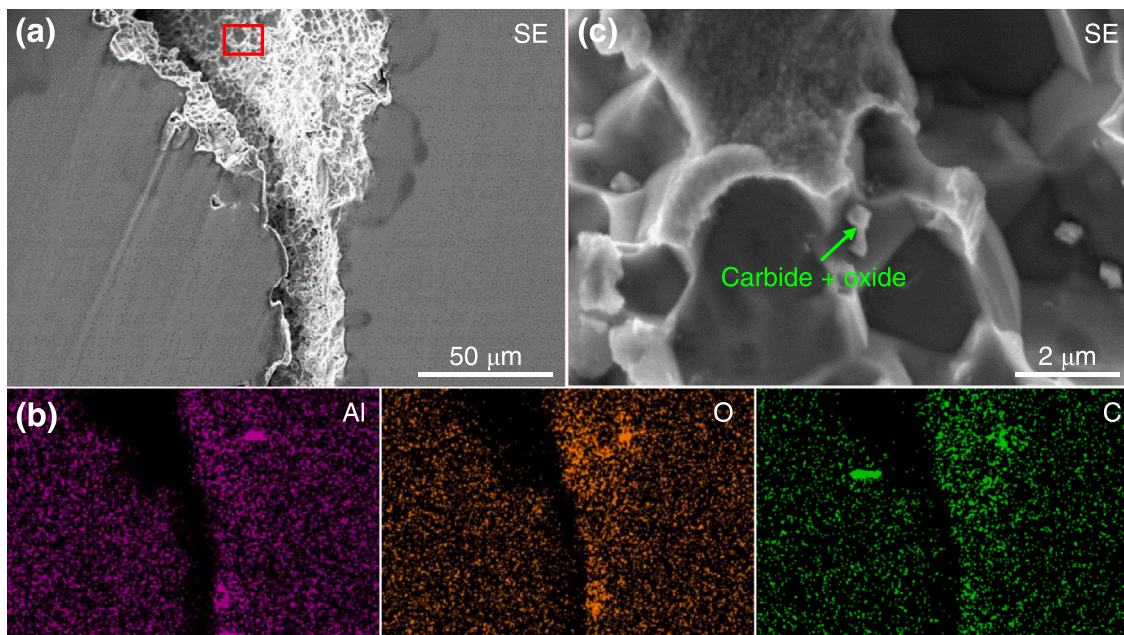


**Fig. 11.** Solid-state cracking in the as-printed DED sample. (a) SE-SEM image and (b) the corresponding EDS maps; (c) SE-SEM image shows the enlarged region marked in (a).

dip cracking) [13].

In the case of AM, the iterative dissolution and re-precipitation of  $\gamma'$  phases in the as-deposited layer are likely to occur when they are subjected to thermal cycles upon the subsequent layer deposition, which is similar to the strain-age cracking formed during the post-weld heat treatment [17]. Additionally, when the deposit layer cools down to a temperature within DTR, an intrinsic ductility drop occurs. Meanwhile, the process induced thermal stresses might promote grain boundary sliding and intergranular strain concentration [13,14]. Once the localized strain exceeds a threshold value, cracking initiates readily due to the low ductility. The already formed hot crack can also be the source of ductility dip cracking, *i.e.*, solid-state cracking may act as a supplement to the propagation of a pre-existing hot crack [14].

Furthermore, impurities such as oxygen can also cause grain boundary embrittlement and promote the initiation and/or propagation of cracks. Oxygen diffusion into the grain boundaries favors the dynamic grain boundary embrittlement, which can aid in the crack propagation [14]. While characterization of the oxides presenting at the cracked grain boundaries in laser additive manufactured IN738 alloys has been widely reported in literature, there is still a large discrepancy about the reported oxide composition. Unlike the as-reported Al/Si/W oxides [54] or Ni/Mo oxides [55], the intergranular segregation of Al, O, and C (Fig. 11b) as well as the carbide/oxide heterostructures at a cracked grain boundary (Fig. 11c) in our DED sample are noticeable. The formation mechanism of such heterostructure is understood to occur as following. The Al atoms in the melt pool are oxidized to alumina particles, which then act as heterogeneous nucleation sites for the formation of carbides during solidification [56]. The carbide/oxide heterostructures with intrinsically high hardness and modulus [54,55] bring forth the localized stress/strain concentration and dislocation tangles (Fig. 6b), increasing the susceptibility to cracking.

#### 4.2.3. Driving force for cracking

In Fig. 2b, the crack network in DED sample is seen to extend along both the longitudinal and the transverse directions. As stated in a previous study, transverse tensile stresses lead to longitudinal weld cracking [57]. During the DED process, thermal shrinkage constricted by the already deposited layers and the base plate results in intensive tensile stresses on the top deposited layers [9,25].

Such stresses can be relieved by the creep deformation of the  $\gamma$  dendrites above their solvus temperature [17]. However, below the  $\gamma'$  solvus, the phase transition stresses induced by a fast  $\gamma'$  precipitation make a significant contribution to the driving force for cracking. Preheating lowers the cooling rate after solidification and the  $\gamma'$  precipitation rate simultaneously [18]. Thus, the level of  $\gamma'$  precipitation induced stresses can be qualitatively estimated by the cooling rate  $C_{\gamma'}$  at the  $\gamma'$  solvus, which has the following empirical relationship with the  $\gamma'$  size [58]:

$$d_0 = qC_{\gamma'}^{-p} \quad (3)$$

where  $d_0$  is the initial  $\gamma'$  diameter (in nm) precipitating just below the  $\gamma'$  solvus; the constant values  $q = 442.5$  and  $p = 0.4605$  of U720LI superalloys [59] are adopted here. It should be emphasized that the size of the  $\gamma'$  in the EB-PBF sample measured from Fig. 5e is different from  $d_0$ , because  $\gamma'$  particles grow continuously under the long preheating duration ( $\sim 5$  h) at  $\sim 950$  °C during the entire EB-PBF process. Then  $d_0$  is derived according to the well-known LSW theory [60,61]:

$$d^3 - d_0^3 = kt \quad (4)$$

where  $d$  is the  $\gamma'$  diameter after coarsening for a period time  $t$  and  $k$  is the temperature-dependent coarsening rate. Using  $d = \sim 152$  nm and  $k = 2.1 \times 10^5 \text{ nm}^3 \cdot \text{h}^{-1}$  predicted by the JMatPro software,  $d_0$  and  $C_{\gamma'}$  of the EB-PBF sample are estimated to be  $\sim 135$  nm and  $\sim 13 \text{ K} \cdot \text{s}^{-1}$  by using Eqs. (1) and (2), respectively. For the DED sample without preheating, the as-precipitated  $\gamma'$  size is assumed to be identical to that in the final

product. Regarding the different  $\gamma'$  sizes in the DC and IR (Fig. 5b),  $C_{\gamma'}$  of the DED sample is calculated spanning from 241 to  $1170 \text{ K} \cdot \text{s}^{-1}$ , much higher than that of the EB-PBF sample. Therefore, it is predicted that the phase transition stresses accompanied by  $\gamma'$  precipitation are much lower in the EB-PBF sample than in the DED sample.

The built-in microscopic defects as well as the development of thermal stresses during solidification and subsequent cooling process can lead to residual stresses in the final part [9]. To evaluate the level of residual stresses in the as-printed DED and EB-PBF samples, a post-printing solutionizing heat treatment (SHT) at  $1120$  °C for  $0.5$  h in air was employed and the microstructure was examined by EBSD. For the DED sample, the solutionizing annealing triggers recrystallization (Figs. 12a and 12c) and results in slightly stronger texture than its as-printed counterpart, probably due to the formation of coarser grains with almost no intragranular misorientations. Plenty of annealing twins, corresponding to the peak near  $60^\circ$  in the misorientation angle histogram (Fig. 12e), are discernable inside the recrystallized grains. The higher stored deformation energy associated with high density of dislocations in the as-printed DED sample is responsible for the recrystallization [62]. For the EB-PBF sample, instead, no recrystallization nucleus is detected and the DS microstructure is preserved after annealing (Figs. 12b and 12d), indicating lower density of microscopic defects, lower process-induced thermal stresses, and possibly dynamic recovery due to the long-term preheating [63].

#### 4.3. Simultaneous achievement of cracking prevention and columnar dendrite growth

In this work, we have demonstrated that a crack-free directionally solidified columnar dendritic microstructure of non-weldable DS IN738 superalloys with reasonable mechanical performance is achievable through the EB-PBF approach with dedicatedly tuned process parameters such as input power and scanning speed. The underlying mechanism is schematically illustrated in Fig. 13.

In the previous sections, the cooling rates (indicated by the arrows on the cooling curves) at the liquid/solid interface ( $C_{1/s}$ ) and the  $\gamma'$  solvus ( $C_{\gamma'}$ ) for both the DED and the EB-PBF processes, where  $C_{1/s, \text{DED}} < C_{1/s, \text{EB-PBF}}$  and  $C_{\gamma', \text{DED}} > C_{\gamma', \text{EB-PBF}}$ , have been estimated. The high cooling rate at the liquid/solid interface not only mitigates the elemental segregation into IRs and the grain boundaries in the EB-PBF products, but also eliminates the formation of low melting point  $\gamma/\gamma'$  eutectics, resulting in an effective suppression of the hot cracking. Moreover, preheating of the base plate significantly reduces the stored deformation energy in the as-printed EB-PBF product, which is the driving force for both cracking and recrystallization. Meanwhile, the shallow melt pool with high width-to-depth ratio during the EB-PBF process creates a steep and unidirectional temperature gradient, which facilitates the epitaxial growth of columnar dendrites along BD. Besides, the vacuum environment enforced during the EB-PBF process contributes to the minimization of oxides and oxygen impurity, further lowering the risk of solid-state cracking.

## 5. Conclusions

A comparative study on AM of non-weldable IN738 superalloy manufactured through DED and EB-PBF is performed to gain a better understanding of the competition between cracking suppression and the directional growth of columnar dendrites. It is demonstrated that the properly controlled temperature gradient and cooling rates at the liquid/solid interface ( $C_{1/s}$ ) and  $\gamma'$  solvus ( $C_{\gamma'}$ ) are the most important factors. The EB-PBF method has advantages over the DED in meeting these conditions simultaneously. On the one hand, a high  $C_{1/s}$  is preferential for suppressing the elemental segregation that improves the resistance to hot cracking. Preheating near the upper bound of DTR and thus low  $C_{\gamma'}$  are necessary to reduce the driving force for cracking. On the other hand, a shallow melt pool is necessary to create a steep and

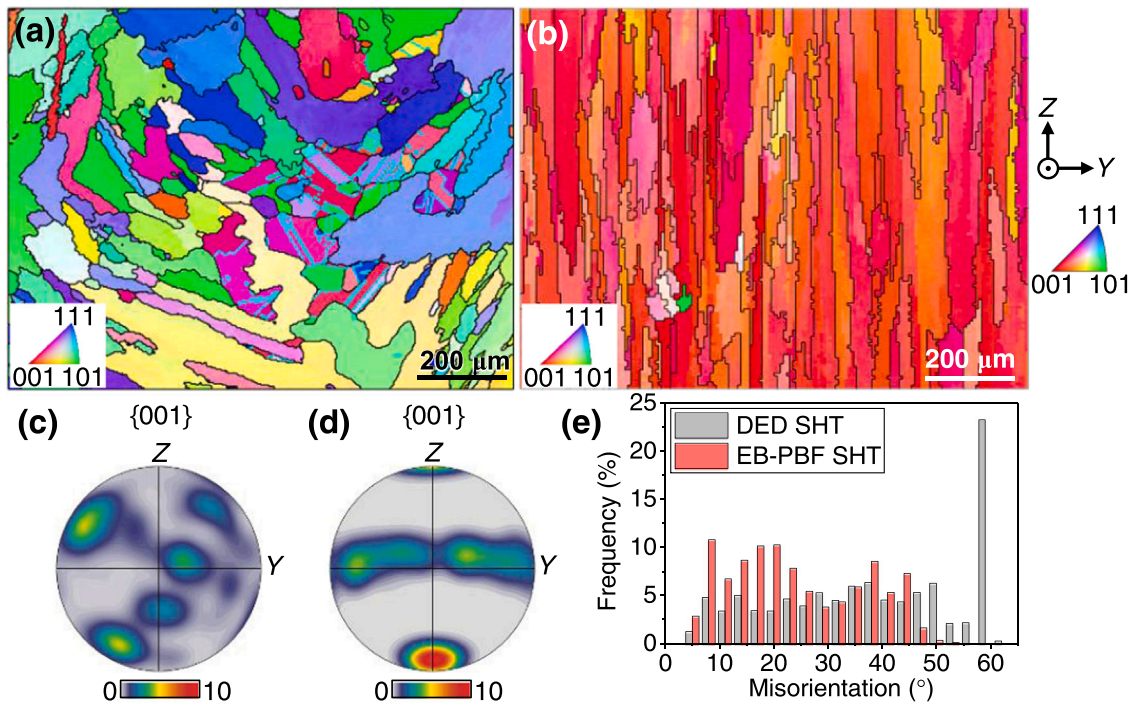


Fig. 12. Microstructural evolution after post-process solutionizing heat treatment. EBSD IPF-Z map and the corresponding inverse pole figure of the solutionized (a, c) DED and (b, d) EB-PBF samples. The {111} twin boundaries are depicted by cyan lines in (a). (e) A statistical analysis of the boundary misorientation angle distribution in two solutionized samples.

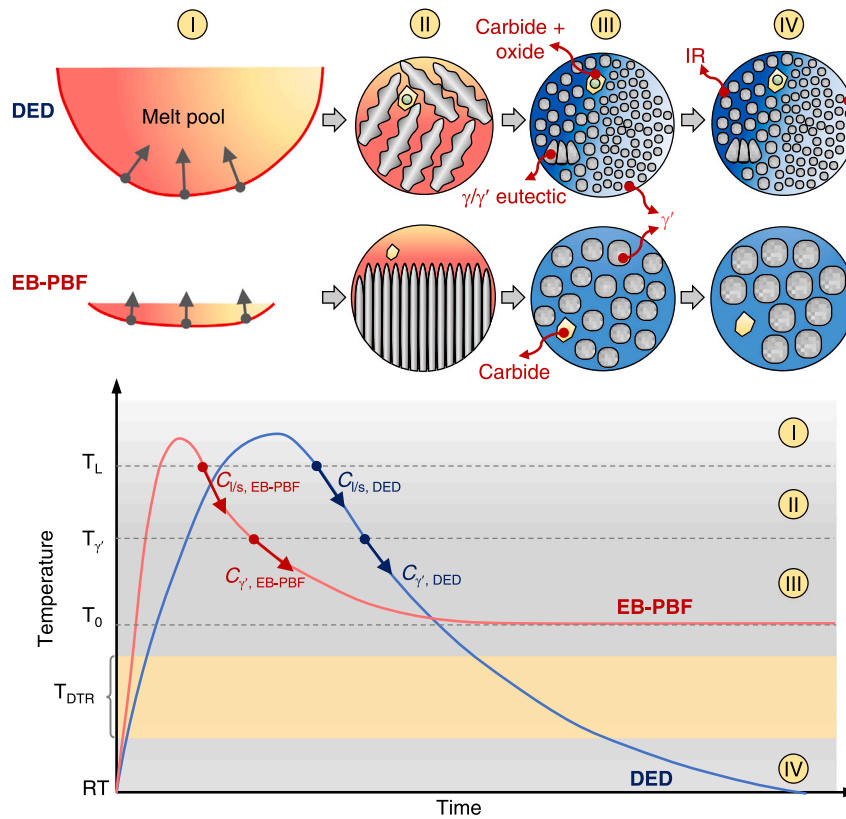


Fig. 13. Schematic illustration of the solidification and cooling processes of DED and EB-PBF shows the microstructural evolution and estimated thermal cycle curves. The melt pool starts to solidify with the nucleation of carbides and the growth of  $\gamma$  dendrites (state I and II) accompanied by solute partitioning; Below the  $\gamma'$  solvus ( $T_\gamma$ ),  $\gamma'$  rapidly precipitates (state III);  $\gamma'$  coarsening in the EB-PBF sample occurs under the long-term preheating at  $T_0$  (state IV).

unidirectional temperature gradient, which facilitates the directional growth of columnar dendrite along BD. In addition, oxygen that is deleterious to ductility and the cohesion of grain boundaries is minimized with the EB-PBF process. Moreover, the low stored deformation energy in the as-printed EB-PBF product contributes to the survival of DS architecture without recrystallization after SHT, and simplifies the design of the post-printing heat treatment protocol.

### CRedit authorship contribution statement

**Xiaofeng Dang:** Investigation, Methodology, Writing – original draft, Data curation, Visualization. **Yao Li:** Investigation, Methodology, Writing – original draft, Data curation, Visualization. **Kai Chen:** Conceptualization, Supervision, Writing – review & editing. **Upadrasta Ramamurty:** Writing – review & editing. **Sihai Luo:** Funding acquisition, Writing – review & editing. **Xiaoqing Liang:** Writing – review & editing. **Weifeng He:** Supervision, Funding acquisition.

### Declaration of Competing Interest

The authors declare that they have no known competing financial interests or personal relationships that could have appeared to influence the work reported in this paper.

### Data Availability

Data will be made available on request.

### Acknowledgments

This work is supported by National Natural Science Foundation of China (Grant No. 51901026, 51927801, 52005508), the National Science and Technology Major Project of China (Grant No. 2019-IV-003-0070) and the Key Research and Development Program of Shaanxi Province (Grant No. 2022GY-383). SL was supported by the Young Elite Scientist Sponsorship Program by CAST (Grant No. 20200321). UR's work was supported by Agency for Science, Technology and Research (A\*STAR) of Singapore via the Structural Metal Alloys Programme (Grant No. A18B1b0061).

### Appendix A. Supporting information

Supplementary data associated with this article can be found in the online version at [doi:10.1016/j.addma.2022.103095](https://doi.org/10.1016/j.addma.2022.103095).

### References

- [1] Y.M. Wang, T. Voisin, J.T. McKeown, J. Ye, N.P. Calta, Z. Li, Z. Zeng, Y. Zhang, W. Chen, T.T. Roehling, R.T. Ott, M.K. Santala, P.J. Depond, M.J. Matthews, A. V. Hamza, T. Zhu, Additively manufactured hierarchical stainless steels with high strength and ductility, *Nat. Mater.* 17 (2018) 63–71, <https://doi.org/10.1038/nmat5021>.
- [2] D. Zhang, D. Qiu, M.A. Gibson, Y. Zheng, H.L. Fraser, D.H. StJohn, M.A. Easton, Additive manufacturing of ultrafine-grained high-strength titanium alloys, *Nature* 576 (2019) 91–95, <https://doi.org/10.1038/s41586-019-1783-1>.
- [3] C. Panwisawas, Y.T. Tang, R.C. Reed, Metal 3D printing as a disruptive technology for superalloys, *Nat. Commun.* 11 (2020) 2327, <https://doi.org/10.1038/s41467-020-16188-7>.
- [4] E. Chauvet, C. Tassin, J.-J. Blandin, R. Dendievel, G. Martin, Producing Ni-base superalloys single crystal by selective electron beam melting, *Scr. Mater.* 152 (2018) 15–19, <https://doi.org/10.1016/j.scriptamat.2018.03.041>.
- [5] Y. Li, W. Kan, Y. Zhang, M. Li, X. Liang, Y. Yu, F. Lin, Microstructure, mechanical properties and strengthening mechanisms of IN738LC alloy produced by electron beam selective melting, *Addit. Manuf.* 47 (2021), 102371, <https://doi.org/10.1016/j.addma.2021.102371>.
- [6] C. Körner, M. Ramsperger, C. Meid, D. Bürger, P. Wollgramm, M. Bartsch, G. Eggeler, Microstructure and mechanical properties of CMSX-4 single crystals prepared by additive manufacturing, *Metall. Mater. Trans. A* 49 (2018) 3781–3792, <https://doi.org/10.1007/s11661-018-4762-5>.
- [7] P. Kontis, E. Chauvet, Z. Peng, J. He, A.K. da Silva, D. Raabe, C. Tassin, J.-J. Blandin, S. Abed, R. Dendievel, B. Gault, G. Martin, Atomic-scale grain boundary engineering to overcome hot-cracking in additively-manufactured superalloys, *Acta Mater.* 177 (2019) 209–221, <https://doi.org/10.1016/j.actamat.2019.07.041>.
- [8] Y. Li, K. Chen, N. Tamura, Mechanism of heat affected zone cracking in Ni-based superalloy DZ125L fabricated by laser 3D printing technique, *Mater. Des.* 150 (2018) 171–181, <https://doi.org/10.1016/j.matdes.2018.04.032>.
- [9] E. Chauvet, P. Kontis, E.A. Jäggle, B. Gault, D. Raabe, C. Tassin, J.-J. Blandin, R. Dendievel, B. Vayre, S. Abed, G. Martin, Hot cracking mechanism affecting a non-weldable Ni-based superalloy produced by selective electron beam melting, *Acta Mater.* 142 (2018) 82–94, <https://doi.org/10.1016/j.actamat.2017.09.047>.
- [10] P. Fernandez-Zelaia, M.M. Kirka, A.M. Rossy, Y. Lee, S.N. Dreypondt, Nickel-based superalloy single crystals fabricated via electron beam melting, *Acta Mater.* 216 (2021), 117133, <https://doi.org/10.1016/j.actamat.2021.117133>.
- [11] A. De Luca, C. Kenel, S. Griffiths, S.S. Joglekar, C. Leinenbach, D.C. Dunand, Microstructure and defects in a Ni-Cr-Al-Ti  $\gamma/\gamma'$  model superalloy processed by laser powder bed fusion, *Mater. Des.* 201 (2021), 109531, <https://doi.org/10.1016/j.matdes.2021.109531>.
- [12] S.P. Murray, K.M. Pusch, A.T. Polonsky, C.J. Torbett, G.G.E. Seward, N. Zhou, S.A. J. Forsik, P. Nandwana, M.M. Kirka, R.R. Dehoff, W.E. Slye, T.M. Pollock, A defect-resistant Co-Ni superalloy for 3D printing, *Nat. Commun.* 11 (2020) 4975, <https://doi.org/10.1038/s41467-020-18775-0>.
- [13] D. Qian, J. Xue, A. Zhang, Y. Li, N. Tamura, Z. Song, K. Chen, Statistical study of ductility-dip cracking induced plastic deformation in polycrystalline laser 3D printed Ni-based superalloy, *Sci. Rep.* 7 (2017) 2859, <https://doi.org/10.1038/s41598-017-03051-x>.
- [14] X. Zhang, H. Chen, L. Xu, J. Xu, X. Ren, X. Chen, Cracking mechanism and susceptibility of laser melting deposited Inconel 738 superalloy, *Mater. Des.* 183 (2019), 108105, <https://doi.org/10.1016/j.matdes.2019.108105>.
- [15] M. Cloots, P.J. Uggowitzer, K. Wegener, Investigations on the microstructure and crack formation of IN738LC samples processed by selective laser melting using Gaussian and doughnut profiles, *Mater. Des.* 89 (2016) 770–784, <https://doi.org/10.1016/j.matdes.2015.10.027>.
- [16] T. DebRoy, T. Mukherjee, H.L. Wei, J.W. Elmer, J.O. Milewski, Metallurgy, mechanistic models and machine learning in metal printing, *Nat. Rev. Mater.* 6 (2020) 48–68, <https://doi.org/10.1038/s41578-020-00236-1>.
- [17] L.C. Lim, J.-Z. Yi, N. Liu, Mechanism of post-weld heat treatment cracking in Rene 80 nickel based superalloy, *Mater. Sci. Technol.* 18 (2013) 407–412, <https://doi.org/10.1179/026708302225001633>.
- [18] J. Xu, X. Lin, P. Guo, Y. Hu, X. Wen, L. Xue, J. Liu, W. Huang, The effect of preheating on microstructure and mechanical properties of laser solid forming IN-738LC alloy, *Mater. Sci. Eng. A* 691 (2017) 71–80, <https://doi.org/10.1016/j.msea.2017.03.046>.
- [19] W. Wang, W. Lin, R. Yang, Y. Wu, J. Li, Z. Zhang, Z. Zhai, Mesoscopic evolution of molten pool during selective laser melting of superalloy Inconel 738 at elevating preheating temperature, *Mater. Des.* 213 (2022), 110355, <https://doi.org/10.1016/j.matdes.2021.110355>.
- [20] Y. Danis, C. Arvieu, E. Lacoste, T. Larrouy, J.-M. Quenisset, An investigation on thermal, metallurgical and mechanical states in weld cracking of Inconel 738LC superalloy, *Mater. Des.* 31 (2010) 402–416, <https://doi.org/10.1016/j.matdes.2009.05.041>.
- [21] M. Gäumann, C. Bezençon, P. Canalis, W. Kurz, Single-crystal laser deposition of superalloys: processing-microstructure maps, *Acta Mater.* 49 (2001) 1051–1062, [https://doi.org/10.1016/s1359-6454\(00\)00367-0](https://doi.org/10.1016/s1359-6454(00)00367-0).
- [22] S. Kou, *Welding Metallurgy*, second ed., John Wiley & Sons, Inc, Hoboken, New Jersey, 2002.
- [23] T. DebRoy, H.L. Wei, J.S. Zuback, T. Mukherjee, J.W. Elmer, J.O. Milewski, A. M. Beese, A. Wilson-Heid, A. De, W. Zhang, Additive manufacturing of metallic components – process, structure and properties, *Prog. Mater. Sci.* 92 (2018) 112–224, <https://doi.org/10.1016/j.pmatsci.2017.10.001>.
- [24] S.-Y. Im, S.-Y. Jun, J.-W. Lee, J.-H. Lee, B.-S. Lee, H.-J. Lee, H.-U. Hong, Unidirectional columnar microstructure and its effect on the enhanced creep resistance of selective electron beam melted Inconel 718, *J. Alloy. Compd.* 817 (2020), 153320, <https://doi.org/10.1016/j.jallcom.2019.153320>.
- [25] Y. Li, D. Qian, J. Xue, J. Wan, A. Zhang, N. Tamura, Z. Song, K. Chen, A synchrotron study of defect and strain inhomogeneity in laser-assisted three-dimensionally-printed Ni-based superalloy, *Appl. Phys. Lett.* 107 (2015), 181902, <https://doi.org/10.1063/1.4934839>.
- [26] Y. Li, K. Chen, R.L. Narayan, U. Ramamurty, Y. Wang, J. Long, N. Tamura, X. Zhou, Multi-scale microstructural investigation of a laser 3D printed Ni-based superalloy, *Addit. Manuf.* 34 (2020), 101220, <https://doi.org/10.1016/j.addma.2020.101220>.
- [27] M. Ramsperger, R.F. Singer, C. Körner, Microstructure of the nickel-base superalloy CMSX-4 fabricated by selective electron beam melting, *Metall. Mater. Trans. A* 47 (2016) 1469–1480, <https://doi.org/10.1007/s11661-015-3300-y>.
- [28] Y. Yao, C. Xing, H. Peng, H. Guo, B. Chen, Solidification microstructure and tensile deformation mechanisms of selective electron beam melted Ni3Al-based alloy at room and elevated temperatures, *Mater. Sci. Eng. A* 802 (2021), 140629, <https://doi.org/10.1016/j.msea.2020.140629>.
- [29] X. Dang, Y. Li, K. Chen, S. Luo, X. Liang, W. He, Insight into the interfacial architecture of a hybrid additively-manufactured stainless steel/Ni-based superalloy bimetal, *Mater. Des.* 216 (2022), 110595, <https://doi.org/10.1016/j.matdes.2022.110595>.
- [30] Z. Zhou, L. Huang, Y. Shang, Y. Li, L. Jiang, Q. Lei, Causes analysis on cracks in nickel-based single crystal superalloy fabricated by laser powder deposition additive manufacturing, *Mater. Des.* 160 (2018) 1238–1249, <https://doi.org/10.1016/j.matdes.2018.10.042>.
- [31] N. Lu, Z. Lei, K. Hu, X. Yu, P. Li, J. Bi, S. Wu, Y. Chen, Hot cracking behavior and mechanism of a third-generation Ni-based single-crystal superalloy during directed

- energy deposition, *Addit. Manuf.* 34 (2020), 101228, <https://doi.org/10.1016/j.addma.2020.101228>.
- [32] J.-W. Park, J.M. Vitek, S.S. Babu, S.A. David, Stray grain formation, thermomechanical stress and solidification cracking in single crystal nickel base superalloy welds, *Sci. Technol. Weld. Join.* 9 (2004) 472–482, <https://doi.org/10.1179/136217104225021841>.
- [33] S.-H. Li, P. Kumar, S. Chandra, U. Ramamurty, Directed energy deposition of metals: processing, microstructures, and mechanical properties, *Int. Mater. Rev.* (2022), <https://doi.org/10.1080/09506608.2022.2097411>. In press.
- [34] A. Kermanpur, N. Varahaam, E. Engilehei, M. Mohammadzadeh, P. Davami, Directional solidification of Ni base superalloy IN738LC to improve creep properties, *Mater. Sci. Technol.* 16 (2013) 579–586, <https://doi.org/10.1179/026708300101508117>.
- [35] N. Perevoshchikova, J. Rigaud, Y. Sha, M. Heilmaier, B. Finnin, E. Labelle, X. Wu, Optimisation of selective laser melting parameters for the Ni-based superalloy IN-738 LC using Doehlert's design, *Rapid Prototyp. J.* 23 (2017) 881–892, <https://doi.org/10.1108/rpj-04-2016-0063>.
- [36] D.M. Norfleet, D.M. Dimiduk, S.J. Polasik, M.D. Uchic, M.J. Mills, Dislocation structures and their relationship to strength in deformed nickel microcrystals, *Acta Mater.* 56 (2008) 2988–3001, <https://doi.org/10.1016/j.actamat.2008.02.046>.
- [37] A. Ramakrishnan, G.P. Dinda, Direct laser metal deposition of Inconel 738, *Mater. Sci. Eng. A* 740–741 (2019) 1–13, <https://doi.org/10.1016/j.msea.2018.10.020>.
- [38] X. Zhang, Z. Chai, H. Chen, J. Xu, L. Xu, H. Lu, X. Chen, A novel method to prevent cracking in directed energy deposition of Inconel 738 by in-situ doping Inconel 718, *Mater. Des.* 197 (2021), 109214, <https://doi.org/10.1016/j.matdes.2020.109214>.
- [39] L. Rickenbacher, T. Etter, S. Hövel, K. Wegener, High temperature material properties of IN738LC processed by selective laser melting (SLM) technology, *Rapid Prototyp. J.* 19 (2013) 282–290, <https://doi.org/10.1108/13552541311323281>.
- [40] L. Scime, J. Beuth, Using machine learning to identify in-situ melt pool signatures indicative of flaw formation in a laser powder bed fusion additive manufacturing process, *Addit. Manuf.* 25 (2019) 151–165, <https://doi.org/10.1016/j.addma.2018.11.010>.
- [41] C. Zhao, N.D. Parab, X. Li, K. Fezzaa, W. Tan, A.D. Rollett, T. Sun, Critical instability at moving keyhole tip generates porosity in laser melting, *Science* 370 (2020) 1080–1086, <https://doi.org/10.1126/science.abd1587>.
- [42] J.M. Vitek, The effect of welding conditions on stray grain formation in single crystal welds – theoretical analysis, *Acta Mater.* 53 (2005) 53–67, <https://doi.org/10.1016/j.actamat.2004.08.039>.
- [43] N. Raghavan, R. Dehoff, S. Pannala, S. Simunovic, M. Kirka, J. Turner, N. Carlson, S.S. Babu, Numerical modeling of heat-transfer and the influence of process parameters on tailoring the grain morphology of IN718 in electron beam additive manufacturing, *Acta Mater.* 112 (2016) 303–314, <https://doi.org/10.1016/j.actamat.2016.03.063>.
- [44] Z. Lei, N. Lu, X. Yu, Epitaxy and new stray grain formation mechanism during epitaxial laser melting deposition of Inconel 718 on directionally solidified nickel-based superalloys, *J. Manuf. Process* 42 (2019) 11–19, <https://doi.org/10.1016/j.jmapro.2019.04.016>.
- [45] Y. Li, K. Chen, X. Dang, F. Zhang, N. Tamura, C.-S. Ku, H. Kang, H.-R. Wenk, XtalCAMP: a comprehensive program for the analysis and visualization of scanning Laue X-ray micro-/nanodiffraction data, *J. Appl. Cryst.* 53 (2020) 1392–1403, <https://doi.org/10.1107/s1600576720010882>.
- [46] R. Burgel, P.D. Portella, J. Preuhs, Recrystallization in single crystals of nickel base superalloys, *Superalloys* (2000) 229–238, [https://doi.org/10.7449/2000/Superalloys\\_2000\\_229\\_238](https://doi.org/10.7449/2000/Superalloys_2000_229_238).
- [47] Y.-J. Liang, X. Cheng, J. Li, H.-M. Wang, Microstructural control during laser additive manufacturing of single-crystal nickel-base superalloys: New processing–microstructure maps involving powder feeding, *Mater. Des.* 130 (2017) 197–207, <https://doi.org/10.1016/j.matdes.2017.05.066>.
- [48] G.L. Knapp, N. Raghavan, A. Plotkowski, T. DeRoy, Experiments and simulations on solidification microstructure for Inconel 718 in powder bed fusion electron beam additive manufacturing, *Addit. Manuf.* 25 (2019) 511–521, <https://doi.org/10.1016/j.addma.2018.12.001>.
- [49] S.A. David, J.M. Vitek, S.S. Babu, L.A. Boatner, R.W. Reed, Welding of nickel base superalloy single crystals, *Sci. Technol. Weld. Join.* 2 (2013) 79–88, <https://doi.org/10.1179/stw.1997.2.2.79>.
- [50] N. Wang, S. Mokadem, M. Rappaz, W. Kurz, Solidification cracking of superalloy single- and bi-crystals, *Acta Mater.* 52 (2004) 3173–3182, <https://doi.org/10.1016/j.actamat.2004.03.047>.
- [51] N. Saunders, U.K.Z. Guo, X. Li, A.P. Miodownik, J.P. Schillé, Using JMatPro to model materials properties and behavior, *JOM* 55 (2003) 60–65, <https://doi.org/10.1007/s11837-003-0013-2>.
- [52] Y. Lei, K. Aoyagi, K. Aota, K. Kuwabara, A. Chiba, Critical factor triggering grain boundary cracking in non-weldable superalloy Alloy713ELC fabricated with selective electron beam melting, *Acta Mater.* 208 (2021), 116695, <https://doi.org/10.1016/j.actamat.2021.116695>.
- [53] O.A. Ojo, N.L. Richards, M.C. Chaturvedi, Study of the fusion zone and heat-affected zone microstructures in tungsten inert gas-welded INCONEL 738LC superalloy, *Metall. Mater. Trans. A* 37 (2006) 421–433, <https://doi.org/10.1007/s11661-006-0013-2>.
- [54] C. Qiu, H. Chen, Q. Liu, S. Yue, H. Wang, On the solidification behaviour and cracking origin of a nickel-based superalloy during selective laser melting, *Mater. Charact.* 148 (2019) 330–344, <https://doi.org/10.1016/j.matchar.2018.12.032>.
- [55] K. Ryou, B. Yoo, P.-P. Choi, On the oxygen-induced hot cracking in a direct laser deposited Ni-based superalloy, *Scr. Mater.* 196 (2021), 113751, <https://doi.org/10.1016/j.scriptamat.2021.113751>.
- [56] G.-D. Zhao, X.-M. Zang, W.-R. Sun, Role of carbon in modifying solidification and microstructure of a Ni-based superalloy with high Al and Ti contents, *J. Iron Steel Res. Int.* 28 (2020) 98–110, <https://doi.org/10.1007/s42243-020-00408-x>.
- [57] S.S. Babu, S.A. David, J.W. Park, J.M. Vitek, Joining of nickel base superalloy single crystals, *Sci. Technol. Weld. Join.* 9 (2004) 1–12, <https://doi.org/10.1179/136217104225017080>.
- [58] H. Wu, Z. Huang, N. Zhou, J. Chen, P. Zhou, L. Jiang, A study of solution cooling rate on  $\gamma'$  precipitate and hardness of a polycrystalline Ni-based superalloy using a high-throughput methodology, *Mater. Sci. Eng. A* 739 (2019) 473–479, <https://doi.org/10.1016/j.msea.2018.10.041>.
- [59] D. Furrer,  $\gamma'$  formation in superalloy U720LI, *Scr. Mater.* 40 (1999) 1215–1220, [https://doi.org/10.1016/s1359-6462\(99\)00094-9](https://doi.org/10.1016/s1359-6462(99)00094-9).
- [60] C. Wagner, Theorie der alterung von niederschlägen durch umlösen, *Z. für Elektrochem.* 65 (1961) 581–591, <https://doi.org/10.1002/bbpc.19610650704>.
- [61] I.M. Lifshitz, V.V. Slyozov, The kinetics of precipitation from supersaturated solid solutions, *J. Phys. Chem. Solids* 19 (1961) 35–50, [https://doi.org/10.1016/0022-3697\(61\)90054-3](https://doi.org/10.1016/0022-3697(61)90054-3).
- [62] K. Chen, R.Q. Huang, Y. Li, S.C. Lin, W.X. Zhu, N. Tamura, J. Li, Z.W. Shan, E. Ma, Rafting-enabled recovery avoids recrystallization in 3D-printing-repaired single-crystal superalloys, *Adv. Mater.* 32 (2020), 1907164, <https://doi.org/10.1002/adma.201907164>.
- [63] L.M. Sochalski-Kolbus, E.A. Payzant, P.A. Cornwell, T.R. Watkins, S.S. Babu, R. R. Dehoff, M. Lorenz, O. Ovchinnikova, C. Duty, Comparison of residual stresses in inconel 718 simple parts made by electron beam melting and direct laser metal sintering, *Metall. Mater. Trans. A* 46 (2015) 1419–1432, <https://doi.org/10.1007/s11661-014-2722-2>.